A&A, 713, A260 (2026)
https://doi.org/10.1051/0004-6361/202659081
© The Authors 2026

Astronomy & Astrophysics

Self-consistent 1D modelling of Jupiter's upper atmosphere as an exoplanet analogue

Nils-Martin Robeling[1,⋆], Sudeshna Boro Saikia[1], Gwenaëlle Van Looveren[1], Ivan Stanković[1], Simon Schleich[1], Colin P. Johnstone[2], Manuel Güdel[1], and Kristina Kislyakova[1]

[1] Department of Astrophysics, University of Vienna, Türkenschanzstrasse 17, 1180 Vienna, Austria
[2] International Institute for Applied Systems Analysis, Schloßplatz 1, 2361 Laxenburg, Austria

Received 22 January 2026 / Accepted 21 July 2026

ABSTRACT

Context. Jupiter's upper atmosphere provides a real-world laboratory for validating first-principles models of giant gaseous exoplanets and for constraining the key physical processes that govern them.
Aims. We extended the 1D first-principles thermo-chemical planetary upper atmosphere model Kompot to simulate hydrogen-rich atmospheres of giant exoplanets and benchmarked it against the archetype giant planet Jupiter.
Methods. We modelled a longitudinal and latitudinal average thermal and chemical profile of Jupiter's upper atmosphere by solving the equations of energy balance, photochemical kinetics, hydrodynamics, and vertical transport in a 1D radial atmospheric grid. The thermal properties of the upper atmosphere were determined by a balance between heating from solar X-ray and ultraviolet (XUV), and infrared (IR) radiation, thermal conduction, Joule heating, and radiative cooling due to H_3^+ and CH_4. The model results were compared with Jupiter observations from Galileo, JUNO, and other instruments. The simulation results were also used as input in the radiative transfer module of the TauREx code to simulate Jupiter's infrared transmission spectrum.
Results. Our model reproduces Jupiter's observed upper-atmospheric thermal structure and observed CH_4 volume mixing ratios. The chemical abundances of other gases also exhibit strong agreement with observations and existing photochemical models. Heating and cooling results show that Joule heating is the dominant heating source throughout most of the upper atmosphere. The transmission spectrum indicates the rich presence of CH_4 in the near- and mid-IR wavelength ranges.
Conclusions. Our physically consistent model framework for Jupiter's upper atmosphere provides a validated baseline for future self-consistent simulations of the thermal and chemical structure of a diverse population of hydrogen-rich exoplanet atmospheres.

Key words. radiative transfer – methods: numerical – planets and satellites: atmospheres – planets and satellites: gaseous planets – planets and satellites: individual: Jupiter

1. Introduction

Understanding the processes shaping the thermal and chemical structure of Jupiter's atmosphere is essential, not only for interpreting observations of our Solar System's gas giants but also for modelling the atmospheres of close-in giant exoplanets, such as hot Jupiters. Although hot Jupiters and Jupiter have different temperatures and orbital distances, Jupiter is the closest analogue in mass, radius, and composition for which we have reliable measurements of temperature and chemical abundances. Recently, the *James Webb* Space Telescope (JWST; Gardner et al. 2023) has detected molecules such as CH_4 (Bell et al. 2023), SO_2 (Tsai et al. 2023), CO_2 (JWST Transiting Exoplanet Community Early Release Science Team et al. 2023), and CO (Grant et al. 2023) in the atmospheres of exo-gas giants.

Even though these detections provide insight into exoplanet atmospheric chemistry, observations alone cannot provide significant insight into the thermal profile and energy budget (Schleich et al. 2024). Photochemical kinetics models (e.g. Moses et al. 2005; Tsai et al. 2017; Knížek et al. 2026) are widely used to model the chemical profile of such planets, where the thermal profile is generally an input parameter. Radiative-convective equilibrium (RCE) models (e.g. Amundsen et al. 2014; Baudino et al. 2015; Tremblin 2015) are used to describe the steady-state temperature structure where radiative cooling and convective heating balance in an atmospheric column. RCE models provide a computationally efficient framework for the lower-atmospheric temperature structure, but they are blind to effects such as heating from exothermic chemical reactions, disequilibrium chemistry, radiative cooling, and thermal conduction. Hence, models that solve the coupled hydrodynamics, chemical kinetics, and energy balance equations, benchmarked against Jupiter observations, can be very effective.

Jupiter's upper atmosphere has, over the past decades, been observationally explored by spacecraft and Earth-based telescopes, but the details of its energetics and composition still raise many unresolved questions, especially since these quantities also vary spatiotemporally (Romani et al. 2008; Kim et al. 2020; García Muñoz et al. 2018). More specifically, the H_3^+ temperature of Jupiter can vary spatially by 600 K (Roberts et al. 2025), and the number densities of hydrocarbons such as C_2H_2 and C_2H_6 deviate by up to an order of magnitude, depending on the longitude and latitude. In the upper atmosphere, above the stratospheric haze layer, we face uncertainties and significant variations due to the banded cloud structures and high-speed jet streams and waves that dominate the atmospheric dynamics of Jupiter (Kaspi et al. 2018). In addition to the vertical structure, the effects from deep atmospheric circulation and waves are

⋆ Corresponding author: nils-martin.robeling@univie.ac.at

Open Access article, published by EDP Sciences, under the terms of the Creative Commons Attribution License (https://creativecommons.org/licenses/by/4.0), which permits unrestricted use, distribution, and reproduction in any medium, provided the original work is properly cited.
This article is published in open access under the Subscribe to Open model. Subscribe to A&A to support open access publication.

poorly mapped and difficult to quantify (García-Melendo et al. 2011).

Over the past few decades, a wide array of models has been developed to decipher the structure and energetics of Jupiter's upper atmosphere. Early 1D photochemical and ionospheric models (e.g. Strobel 1973; Gladstone et al. 1996; Perry et al. 1999) established the basic roles of hydrocarbon photolysis and ion–neutral chemistry but generally relied on prescribed temperature profiles and simplified diffusion schemes. Other efforts have increasingly sophisticated chemistry and vertical mixing (e.g. Moses et al. 2005). The thermal structure of Jupiter's upper atmosphere has long been a perplexing problem, as it was too hot for models to be explained solely by solar heating. Several theories, such as heating from gravity waves (Young et al. 1997; Matcheva & Strobel 1999), dissipating and depositing heat, or particle precipitation and auroral heating, are widely discussed (Horanyi et al. 1988). However, it is stated that, for gravity wave heating, the observed quantities are insufficient to achieve the required heating of the order of magnitude. At the same time, auroral, magnetic, and ionospheric models have highlighted the importance of Joule heating and particle precipitation in shaping the thermal structure at high latitudes (Nishida & Watanabe 1981; Grodent et al. 2001). Despite this progress, models attempting to compute both the chemical and the thermal profiles self-consistently are rare. Grodent et al. (2001) present a self-consistent model of the upper atmosphere, from 1 mbar to the exobase, in the auroral regions. However, an average self-consistent radial model of Jupiter's thermal and chemical profile as an exoplanet analogue does not yet exist. This gap becomes increasingly relevant as analogous processes are used to explain the energetics of hot Jupiter atmospheres, yet benchmarked models for Jupiter-like conditions remain limited.

While all the above-mentioned models only capture one dimension, general circulation models (GCMs) can serve as powerful tools for capturing the 3D connections between radiative transfer and large-scale dynamics. The primary advantage of GCMs lies in their ability to simulate horizontal transport. Specifically, they can capture the intense zonal jets and meridional heat redistribution that dominate the upper atmospheric temperature profile of Jupiter's non-auroral regions. For Jupiter, there are multiple GCMs that have effectively simulated the upper atmosphere and its temperature variations, such as Majeed et al. (2005) or Müller-Wodarg et al. (2025). However, incorporating highly detailed calculations of disequilibrium processes, such as comprehensive photochemistry networks and detailed cooling functions, remains computationally prohibitive in a 3D framework. Another caveat is that the regime of exoplanet GCMs usually does not stretch above the homopause, and detailed calculations of disequilibrium processes, such as photochemistry, are primarily done in 1D. While GCMs offer an inherently self-consistent treatment of coupled non-linear dynamics and major energetic inputs (e.g. solar and Joule heating), they trade off microphysical and chemical complexity to remain computationally feasible. This is where 1D models featuring highly detailed, self-consistent vertical physics and complex chemical networks can complement GCMs.

For this work, we extended the 1D atmospheric model Kompot, originally developed for rocky bodies in the Solar System, to gas-giant atmospheres. We set the simulation boundary above the cloud deck, and self-consistently simulated the average thermal and chemical structure of Jupiter's upper atmosphere over the pressure range 10^{-3} to the exobase, treating Jupiter as an exoplanet around a Sun-like star. Our model represents a globally averaged radial atmospheric structure rather than localised or time-dependent conditions. This paper is structured as follows. Section 2 describes the Kompot model, the other methods used, and the assumptions in this work. Section 3 discusses the results, and Section 4 provides the conclusions.

2. Model

The Kompot code is a 1D first-principles model that computes the thermal and chemical structure, as well as the Jeans escape rate, of planetary upper atmospheres. The model does this by solving the hydrodynamical equations coupled with the energy balance and chemistry. In this work, we define the upper atmosphere as the atmospheric layer above the stratospheric haze layer and cloud decks on Jupiter at 10^{-3} bar. As input, Kompot requires a boundary condition comprising molecular abundances, base temperature, eddy diffusion profile, and parameters relevant to Joule and XUV/IR heating, as further discussed in Sect. 2.5. The model's output is a thermal and chemical profile that includes contributions from different heating and cooling sources. The Kompot code was originally developed for rocky planets in the Solar System. This work extends the model to gas giants. For more detailed information about the model, see Johnstone et al. (2018, 2019, 2021). Below, we discuss the key processes involved in Kompot and the modifications made to make it suitable for gas giant atmospheric modelling. This is followed by a discussion on the radiative transfer model used to generate a transmission spectrum from our Kompot simulation.

2.1. Hydrodynamics

While the Kompot code can simulate hydrodynamic atmospheres, in this work we considered the hydrostatic case. This means that in

$$\frac{1}{\rho}\frac{\mathrm{d}\rho}{\mathrm{d}r} = -\frac{1}{T}\frac{\mathrm{d}T}{\mathrm{d}r} - \frac{g}{v_0^2} + \frac{1}{\bar{m}}\frac{\mathrm{d}\bar{m}}{\mathrm{d}r} - \frac{v}{v_0^2}\frac{\mathrm{d}v}{\mathrm{d}r}, \tag{1}$$

where ρ is density in g/cm^3, T is temperature in K, r is radius in cm, g is the gravitational acceleration in cm/s^2, $\bar{m}$ is the mean molecular mass of the gas in Da, v is the bulk vertical advection speed in m/s, and $v_0^2 = k_B T/\bar{m}$. We set $v = 0$. This effectively gives us the differential of the density structure as

$$\frac{1}{\rho}\frac{\mathrm{d}\rho}{\mathrm{d}r} = -\frac{1}{T}\frac{\mathrm{d}T}{\mathrm{d}r} - \frac{g}{v_0^2} + \frac{1}{\bar{m}}\frac{\mathrm{d}\bar{m}}{\mathrm{d}r}, \tag{2}$$

which is then integrated from the lower boundary, where the density is calculated based on the input number density, up to the exobase. The exobase is dynamically calculated and is defined as the boundary before a transition into the collisionless regime, where the mean-free path of a particle becomes equal to the scale height of the atmosphere

$$\frac{1}{\sqrt{2}\sigma n} = \frac{k_B T}{\bar{m} g}, \tag{3}$$

where σ is the collisional cross-section area of molecular hydrogen, n is the number density, and k_B is the Boltzmann constant. This is also known as the altitude at which the Knudsen number, the ratio of the mean-free path to the scale height, equals 1. Above the exobase, the particles no longer follow a Maxwellian velocity distribution, and Jeans escape becomes increasingly relevant.

2.2. Chemistry

The chemical network used in Kompot includes neutral, ionic, and photochemical reactions, as well as hydrocarbon chemistry up to C_2H_6. Reaction rate coefficients are primarily taken from the Kinetic Database for Astrochemistry (KIDA) (Wakelam et al. 2012), supplemented by additional sources and other networks such as those of Yung et al. (2009), García Muñoz (2007), Richards & Voglozin (2011), Fox (2015), and VULCAN (Tsai et al. 2017) where necessary. We use cross-sections for XUV photochemistry from PHIDRATES (Herbst 1985; Huebner & Mukherjee 2015).

The coupled set of continuity equations governing the transport and transformation of chemical species is solved using a Rosenbrock-type semi-implicit integrator (Sandu et al. 1997). This type of solver is well-suited to stiff systems, characterised by the coexistence of fast radical reactions and slow photolytic or recombination processes.

2.3. Energy balance

A steady-state model atmosphere requires the balance of heating, cooling, and thermal conduction. In this section, we describe the key processes affecting the thermal structure in our 1D model; for a more detailed description, refer to Johnstone et al. (2018) or references herein. The only free parameters in the heating module are the magnetic field and total Joule heating input energy.

2.3.1. Heating

The heating rate from XUV radiation is obtained using a simplified radiative transfer model. We assign the energy not used in photoreactions from the XUV radiation field to the gas as heat. For each atmospheric layer i, the heating contribution is calculated by summing over all absorption reactions and photon energy bins. The heating contribution accounts for the excess photon energy above the ionisation threshold, weighted by the local photon flux, the bin width in energy space, and the corresponding reaction cross sections, yielding the volumetric heating rate $Q_{XUV,i}$ of layer i.

Heating from photoelectrons, via photoionisation, is calculated following the approach of Schunk & Nagy (1978). The electron temperature characterises the thermal background, while the photoelectron velocity distribution is obtained from their kinetic energy. The first energy bin where the photoelectron flux exceeds the thermal Maxwell-Boltzmann flux is identified as the threshold for heating. This is where the photoelectron population starts dominating over the background thermal electrons. Above this threshold, the energy loss rate of non-thermal electrons is given by Eqs. (9) and (11) of Schunk & Nagy (1978). The corresponding heating rate per atmospheric layer i is then computed using their Eq. (7):

$$\Gamma_{PE,i} = \sum_j P_{e,i}(E_j)\frac{dE}{dx}(E_j)\,dE_{PE}(E_j) + (E_{\min} - E_{\text{therm}})\,\frac{dE}{dx}(E_{\min})P_{e,i}(E_{\min}), \tag{4}$$

where $P_e(E_x)$ is the photoelectron flux spectrum, dE/dx is the energy loss rate, and $E_{\min}$ denotes the first energy bin above the thermal background.

Joule heating in our model is a scaled free parameter following the formalism of Foster et al. (1983). While total Joule heating, Q_j, is a free parameter specified in the initial conditions, the fraction deposited in each layer must still be calculated. We do this by first finding the ion cyclotron frequencies as

$$\omega_{c_i} = \frac{e_i B}{m_i c}, \tag{5}$$

where e_i is the electric charge of species i, B is the magnetic field strength, c is the speed of light, and m_i is the mass of the species. We then move on to find the momentum transfer collisional frequencies for resonant charge exchange as

$$\nu_{in} = \frac{8}{3\sqrt{\pi}} n_n \left[\frac{2k(T_i + T_n)}{m_i}\right]^{1/2} [A' + 3.96B' - B'\log_{10}(T_i + T_n)]^2, \tag{6}$$

where n_n is the neutral density, T_i is the ion temperature, T_n is the neutral temperature, m_i is the mass of the ion, and A' and B' are constants from Schunk & Nagy (2009) that depend on the considered species.

We also add the non-resonant collision frequencies for ion-neutral pairs with $\nu_{in} = C_{in} n_n$, where C is a numerical coefficient from Table 4.4 in Schunk & Nagy (2009). Together with the collision frequencies, we can find the conductivity of the ions as

$$\sigma_i = \frac{n_i e_i^2}{m_i \nu_i}. \tag{7}$$

We put Eqs. (5), (6), and (7) into the following equation to find the Pedersen conductivity via the expression,

$$\sigma_P = \sum \sigma_i \frac{\nu_i^2}{\nu_i^2 + \omega_{c_i}^2}, \tag{8}$$

where i is the considered ion, σ_i is the ion conductivity, ν_i the collision frequency in total for one ion. The above equation is a simplification since the electron contribution is removed because $\nu_e \ll \omega_{c_e}$ in most cases, since electrons are strongly tied to the magnetic field and the collisions are too infrequent to disrupt their gyration, thus keeping terms that are only of order ν_e/ω_{c_e}. After retrieving the Pedersen conductivity, we form the expression for Joule heating,

$$Q_j = \sigma_P E^2, \tag{9}$$

where Q_j is the Joule heating per cell and E is the electric field strength. To estimate the spatial distribution of the Joule heating, we set E=1, following which we only require the shape of the Pedersen conductivity profile to obtain the distribution of the Joule heating across all cells. To obtain the actual energy values per bin we first sum up the contribution across all cells as

$$Q_{rad} = \int^{R_{pl}} 4\pi\sigma_P(r) r^2 dr, \tag{10}$$

to find the final estimate of Q_j per cell by scaling the free parameter, total heating input, to local heating input

$$Q_j \approx \sigma_P \frac{Q_{j,input}}{Q_{rad}}, \tag{11}$$

where $Q_{j,input}$ is the total input Joule heating to the atmosphere. Effectively, this calculates a Pedersen conductivity profile throughout the atmosphere and then distributes the model

Table 1. Model input conditions.

Parameter	Value	Reference	Note
Eddy diffusion profile	See Ref. and Fig. 1 (cm/s^2)	Model A and C from Moses et al. (2005)	Includes K_{zz} = 10^6/10^7
X(H_2)	8.35×10^{-1}	Moses et al. (2005)	Lower boundary mixing ratio
X(He)	1.62×10^{-1}	Moses et al. (2005)	Lower boundary mixing ratio
X(CO)	4.42×10^{-8}	Moses et al. (2005)	Lower boundary mixing ratio
X(N_2)	3×10^{-5}	Moses et al. (2005)	Lower boundary mixing ratio
X(CH_4)	2.1×10^{-3}	Moses et al. (2005)	Lower boundary mixing ratio
X(C_2H_2)	2×10^{-7}	Moses et al. (2005)	Lower boundary mixing ratio
X(C_2H_4)	4×10^{-9}	Moses et al. (2005)	Lower boundary mixing ratio
X(C_2H_6)	8×10^{-6}	Moses et al. (2005)	Lower boundary mixing ratio
n	4.36×10^{16} (cm^{-3})	Galileo probe measurement (Yelle 2001)	Lower boundary number density
T	165 (K)	Galileo probe measurement (Yelle 2001)	Lower boundary temperature
Γ_j	~10^{21} [erg/s]	Müller-Wodarg et al. (2025)	Total Joule heating
B	4.17 [G]	Connerney et al. (2018)	Magnetic field strength
θ_Z	15–75 (60) [∘]	–	Zenith angle (main models)

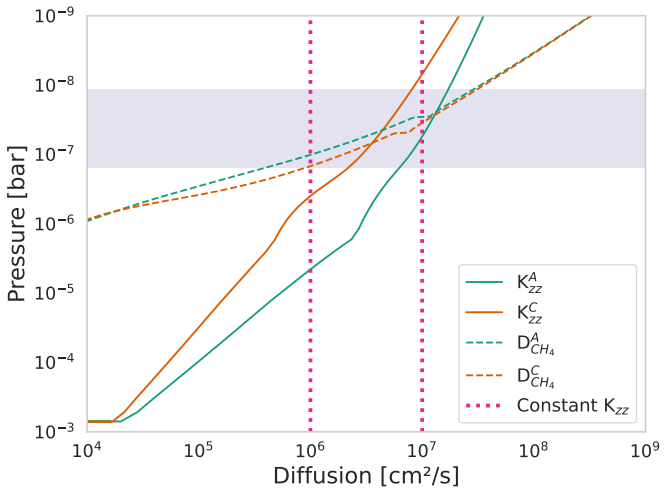

Fig. 1. Molecular and eddy diffusion considered for the different models in this work. The shaded area represents the possibility space of Jupiter's homopause location with results from Sinclair et al. (2020) and Rodríguez-Ovalle et al. (2024).

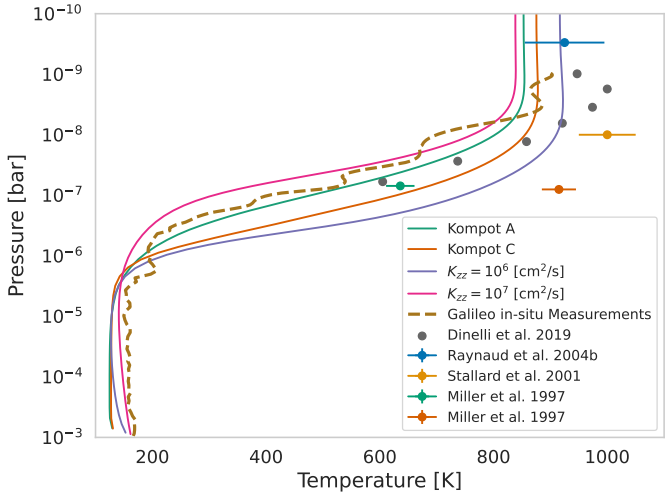

Fig. 2. Thermal profiles of our four models from Kompot. Model A and C use the corresponding K_{zz} from Moses et al. (2005), and the other two models use constant values. Here we compare them with in situ measurements and with different measurements from Earth-based telescopes, as well as with one in situ measurement. The in situ measurement is from the Galileo probe, entering Jupiter's atmosphere at a 5 μm hot spot. The markers with error bars come from different ground-based telescopes measuring Jupiter's auroral regions. Raynaud et al. used the CFHT-FTS (Canada–France–Hawaii Telescope-Fourier transform spectrometer) in the northern hemisphere at 150°-170° System III longitude (Raynaud et al. 2004), Stallard et al. used the CSHELL spectrometer on the NASA-IRTF (Infrared Telescope Facility) (Stallard 2002), and Miller et al. used the UKIRT (United Kingdom Infrared Telescope) (Miller et al. 1997). The grey scatter points from Dinelli et al. (2019) are from the JIRAM (Jovian Infrared Auroral Mapper) on JUNO via retrievals.

input total Joule heating, which is a free parameter, over it. Since the Joule heating profile strongly follows the shape of the Pedersen conductivity profile, we have chosen to include only the Joule heating profile.

Finally, the heating from chemical reactions is calculated by summing the net energy released or absorbed for exothermic and endothermic reactions, each multiplied by the reaction rate per layer, using formation enthalpy values.

Although the Kompot code contains multiple sources of heating, it is imperative to mention that it does not include heating from the particle precipitation prevalent in the auroral regions of Jupiter (Rodríguez-Ovalle et al. 2024), and is thus not suitable for simulating these hotter regions specifically, but rather the horizontally averaged profile.

2.3.2. Cooling

The cooling of Jupiter's upper atmosphere is dominated by two major sources: line cooling from H_3^+, and radiative cooling from CH_4. These two cooling effects operate and dominate in distinct regions. Well below the homopause, where CH_4 does not experience heavy photolysis, radiative cooling from CH_4 dominates, since no other strong cooling sources are available. Line cooling from H_3^+ is first effective above the homopause, where H_3^+ becomes available through interactions with solar photons. The H_3^+ line cooling is handled according to Miller et al. (2013) using the coefficients available in their Table 5, which are then

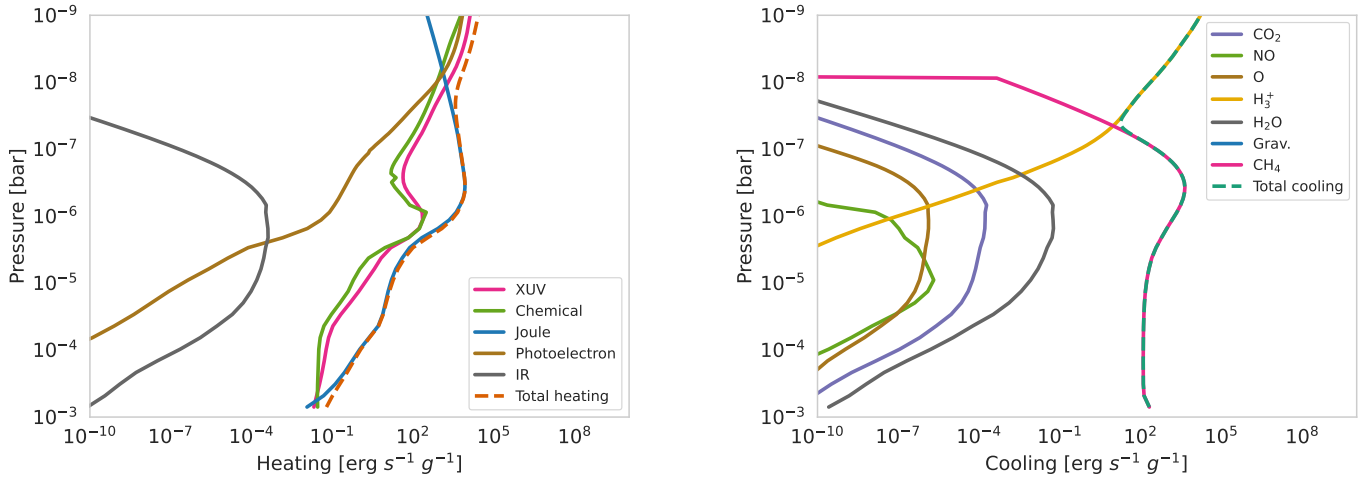

Fig. 3. Total heating and cooling for Model A shown together with the individual processes that contribute towards the total. Left: the constituents of heating together with total heating. Right: the dominant cooling terms are shown together with the total cooling. Please note that gravitational cooling is too low to be present in the plot.

multiplied by a scale factor to account for non-LTE effects and the density of H_3^+. Radiative cooling from CH_4 uses ExoMol (Tennyson et al. 2024) data to fit a function between 1 and 1500 K to the cooling in line with Tennyson et al. (2016). This does not account for non-LTE effects, which is not a big problem for the model since CH_4 cooling dominates below the homopause, where LTE is a good approximation; however, this approximation may make the model slightly cooler. For a more detailed description, refer to Tennyson et al. (2016) or Boro Saikia et al. (in prep.). In addition to line cooling from H_3^+ and radiative cooling from CH_4, there are several other line cooling sources described in the following paragraphs.

We obtain the CO_2 line cooling by first calculating the escape probability, P_{esc}, for each cell, based on the values tabulated in Kumer & James (1974). To then derive the density of excited CO_2 particles, n_{CO_2-vib}, we assume a steady state in accordance with Eq. (37) in Johnstone et al. (2018). The escape probability and density of excited CO_2 particles is subsequently put together with the Einstein coefficient, A_{10}, and the energy lost per emission at 15 μm to form

$$\Lambda_{CO_2} = 1.32510^{-13} n_{CO_2-vib} P_{esc}. \tag{12}$$

Due to the vibrational transition at 5.3 μm, line cooling from NO is calculated in a similar manner to CO_2 cooling described above. The density of NO_{vib}, $n_{NO_{vib}}$ is derived using the methods described in Oberheide et al. (2013), and is then used together with the Einstein coefficient, A_{10}, from the same source to form the expression for the cooling as

$$\Lambda_{NO_{vib}} = 3.75 A_{10} 10^{-13} n_{NO_{vib}}. \tag{13}$$

Line cooling from O is handled as described in Banks & Kockarts (1974), but only cooling due to emission at 63 and 147 μm is considered. This forms the expression for the cooling as

$$\Lambda_O = \frac{1.67 \cdot 10^{-18} e^{(-228/T_i)} + 4.59 \cdot 10^{-20} e^{(-326/T_i)}}{1 + 0.6 e^{(-228/T_i)} + 0.2 e^{(-326/T_i)}} n_O. \tag{14}$$

For cooling due to the emission from the Lyman α line, our calculations follow those of Murray-Clay et al. (2009), resulting in

$$\Lambda_{Ly\text{-}\alpha} = 7.510^{-19} n_H n_e e^{\frac{-118348.0}{T_i}}. \tag{15}$$

Finally, H_2O cooling is expressed as

$$\Lambda_{H_2O} = n_H n_{H_2O} L_{H_2O}, \tag{16}$$

where n_H, and n_{H_2O} is the number density for H and H_2O respectively, and L_{H_2O} is the line coefficient, calculated following the methods of Kasting & Pollack (1983).

2.4. Diffusion

Diffusion in the model is governed by the balance of molecular and eddy diffusion, resulting in a diffusive flux:

$$\Phi_d = n v_d. \tag{17}$$

This is calculated individually for each species, where n is the number density of the species and v_d is the diffusion speed given by

$$v_d = -D\left[\frac{1}{n}\frac{dn}{dr} - \frac{1}{N}\frac{dN}{dr} + \left(1 - \frac{m}{M}\right)\frac{1}{p}\frac{dP}{dr} + \frac{\alpha_T}{T}\frac{dT}{dr}\right] - K_{zz}\left[\frac{1}{n}\frac{dn}{dr} - \frac{1}{N}\frac{dN}{dr}\right], \tag{18}$$

where D is the molecular diffusion coefficient, N is the total gas density, r is the radial distance, m and M are the molecular mass of the considered species and the background gas, respectively, P is the gas pressure, α_T is the thermal diffusion factor, and K_{zz} is the eddy diffusion coefficient. We allow K_{zz} to be a free input parameter in the code, which the user supplies as an altitude-dependent profile.

The molecular diffusion coefficient, however, is not a free parameter. As in Johnstone (2020) the value of D for a specific species in a background gas is calculated as

$$D = \frac{3}{2n(R + r_s)^2}\sqrt{\frac{k_B T}{2\pi}\left(\frac{1}{M} + \frac{1}{m}\right)}, \tag{19}$$

where R is the background gas molecular radius, r_s is the radius or the considered species, following Chapman–Enskog theory (Chapman & Cowling 1970).

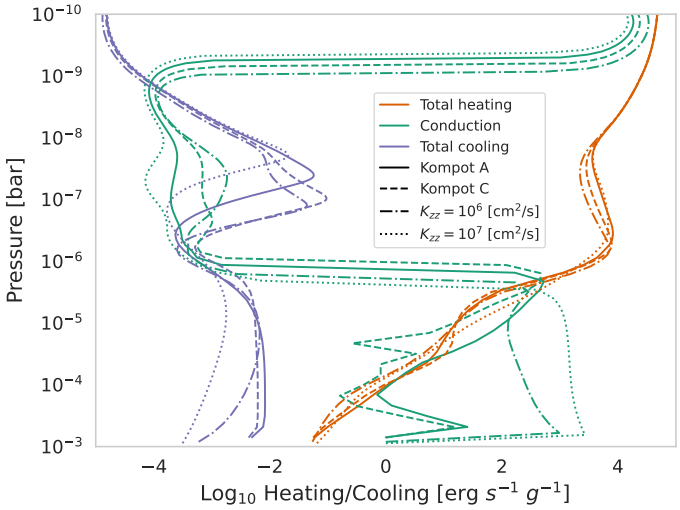

Fig. 4. Total heating, cooling, and conduction for all four models. The cooling curves have been subjected to a sign change to illustrate the balance with conduction, where conduction on the left-hand side of 0 indicates cooling from conduction. Note that heat flux from the bottom boundary is not displayed in total heating, but shows up as a sharp feature in the conduction profile.

Both the molecular and eddy diffusion coefficients are used not only to calculate the diffusive flux but also to determine the location of the homopause, which is important for initialising species densities. The homopause itself is found where the molecular diffusion coefficient is equal to that of the eddy diffusion coefficient, or $K_{zz} = D$. Below, in the homosphere, where the gas is well mixed, the scale height of the mixed gas is used to calculate the initial profile of species densities; the scale heights of individual species are then used in the heterosphere, where the gas is separated into distinct layers. In reality, the homopause is a transition region that does not exist at a single distance; however, since this sharp transition is only an initial condition, treating it as a point in our 1D model is a good approximation.

2.5. Setup

The above set of equations is solved on a finite grid of cells using the numerical solvers described in the appendices of Johnstone et al. (2018). The lower boundary is set to an altitude of 150km, and several ghost cells are added to the grid below the lower boundary for numerical reasons; these cells are not included in the figures presented in this paper. The upper boundary lies at the exobase, which is allowed to vary during the simulation in response to changes in the atmosphere's physical structure. The gas properties at the lower boundary that we assume are the neutral density, temperature, and mixing ratios of the major species. Additional parameters we set include the zenith angle, eddy diffusion coefficients, and the input solar XUV spectra, which are taken from Claire et al. (2012). The input lower boundary conditions are described in Table 1 and Fig. 1. The mixing ratios at our input lower boundary in Table 1 are averages at 1 mbar from the model results of Moses et al. (2005).

The simulation domain between the lower boundary and the exobase is initialised with a uniform temperature gas. The initial vertical profiles of the gas composition are determined by first finding the homopause where $K_{zz} = D$ and then assuming a uniform mixing ratio of the major species below this altitude and each species following its own mass-dependent scale height above this altitude. The Kompot model then evolves the gas properties within the simulation domain in response to the thermal and chemical processes considered, while keeping the lower boundary conditions constant, until the simulation reaches a steady state, which we take as our solution. All neutral, ion, and electron densities not presented in Table 1 are therefore created self-consistently by the photochemical model within Kompot.

Eddy diffusion is one of the major free parameters of the model, since it cannot be derived from physical principles or conditions alone (Lindzen 1981; Strobel et al. 1985). We therefore consider four models that differ only in the assumed eddy diffusion coefficients. The eddy diffusion profiles, A and C, developed by Moses et al. (2005), served different purposes. Profile A was developed to fit the lower end of previously obtained number densities from both observations and models, and profile C was developed to fit the higher end. While profiles A and C feature slightly different chemistry in the original source, we use the same chemical network and mixing ratios for both models. Profile B is intentionally left out because it does not exhibit different chemistry in the original sources, and the coefficient values lie between profiles A and C. We additionally run models with two uniform values of the eddy diffusion coefficients. The vertical profiles of the eddy diffusion coefficients for each model are shown along with the molecular diffusion coefficients for CH_4 in Fig. 1.

2.6. Transmission spectrum

We calculate a transmission spectrum using 1D radiative transfer with the vertical temperature and chemical profiles from the Kompot simulation results of profile A. We use the radiative transfer part of the `TauREx` code (Al-Refaie et al. 2021, 2022). The radiative transfer forward model comprises 157 layers, spanning the pressure domain of the Kompot model ($p_{\rm BOA} \approx 7 \times 10^{-4}$ bar and $p_{\rm TOA} \approx 3 \times 10^{-12}$ bar). We considered absorption cross-sections from the ExoMol project (Tennyson et al. 2020; Chubb et al. 2021), as well as the HITRAN (Gordon et al. 2022) and HITEMP (Rothman et al. 2010) archives. The opacity sources contributing to the optical depth of the forward model include molecular absorption by CH_4 (Yurchenko et al. 2017), CH_3 (Adam et al. 2019), C_2H_2 (Chubb et al. 2020), C_2H_4 (Mant et al. 2018), CO (Li et al. 2015), CO_2 (Yurchenko et al. 2020), and H_2O (Polyansky et al. 2018), collision-induced absorption (CIA) from H_2–H_2 (Abel et al. 2011; Fletcher et al. 2018) and H_2–He (Abel et al. 2012) pairs, as well as Rayleigh scattering as included in `TauREx` (Cox 2015).

3. Results and discussion

3.1. Thermal structure

In Fig. 2, we compare the thermal profiles of our four models with observational data and in situ measurements from Galileo (Yelle 2001). Our models are slightly colder than the measurements at higher pressures below the temperature inversion. This small difference could be due to either the absence of aerosol heating or potential non-LTE effects not included in the model. Around 10^{-6} bar, just below the homopause, the thermal profile plateaus, followed by a thermal inversion. This structure arises because CH_4 is photolysed, thereby stifling its radiative cooling, heating the atmosphere. The upper atmosphere then heats rapidly until it is once again balanced by the emerging H_3^+ cooling, which becomes effective as ionisation increases and H_3^+ becomes available, radiating effectively in the infrared.

Our model reproduces both the location of the thermal inversion and the temperature above it with good precision. Since Jupiter is a well-studied object with data from many different regions and sources, our model cannot agree with all measurements and models simultaneously. The spatial variation in temperature makes it difficult to represent accurately with a 1D model. Because Jupiter also has highly active auroral regions due to its strong magnetic field, it poses an additional challenge. As discussed earlier in Sect. 2.3.1, Kompot does not contain heating from particle precipitation or any other effects attributed to the magnetic field. In addition, upward-propagating waves and large-scale dynamics may transport energy into the upper atmosphere, thereby contributing to local temperature variability that Kompot currently cannot reproduce. It is also worth noting that the Sun's XUV spectrum is highly variable over time, adding another source of temporal variation.

In Fig. 3, we show the heating and cooling components for Model A. As seen on the left-hand side, Joule heating dominates throughout most of the atmosphere, accounting for ∼200 TW when integrated over the total contribution, and is replaced around the homopause by chemical (∼15 TW) and XUV heating (∼10 TW). The physical processes behind this are all connected to the balance between gyrofrequencies and collision frequencies. Where they have similar values, the electrons can move perpendicular to the magnetic field, current flows, and we have resistive heating. Joule heating experiences the drop starting at around 1 μbar because the neutral density drops, causing the ion collision frequency ν_i to decrease, i.e. $\omega_{c_i} \gg \nu_i$. This reduces the denominator in Eq. (8), leading to a decrease in the Pedersen conductivity.

In chemical and XUV heating, we see a drop of about an order of magnitude slightly below the homopause. In this region, the structure changes from well-mixed to layered, causing key absorbers, the heavy hydrocarbons, to stay at higher pressures. As a result, we observe that the heat released upon absorbing XUV radiation decreases. The sudden decline is then quickly recovered when atomic hydrogen, with its large photoabsorption cross-section, becomes more readily available.

The shape of the chemical heating profile has similar origins. At the homopause, key reactions for energy release turn off since ion-neutral chemistry is weakened because of the drop in number density and some reactants, such as CH_4, disappear faster with decreasing pressure than others. These reactions are quickly replaced by dissociative recombination, releasing energy as new hydrogen-based ions, such as H^+, H_2^+, and H_3^+, become available. Because total heating is independent of chemistry, since chemical heating is never the dominant heating source, it is largely unaffected by the eddy diffusion coefficients, as seen in Fig. 4.

Up until the upper parts of the homosphere (P $\sim 10^{-7}$ bar), cooling is heavily dominated by radiative cooling from hydrocarbons, present in this model, is cooling from CH_4, as detailed in Section 2.3.2. Since CH_4 is heavy, it has a small scale height, leading to the quick decrease in density just above the homopause. Together with photolysis that starts in the upper homosphere, these two effects are responsible for CH_4 no longer being available above the homopause. The deficit in CH_4 leads to less cooling because of the number density dependence, and as soon as $X(H_3^+) > X(CH_4)$, line cooling from H_3^+ becomes the dominant cooling mechanism quickly in the right-hand side of Fig. 3.

The balance between heating and cooling, together with conduction, can be seen in Fig. 4. Since conduction depends on the eddy and molecular diffusion coefficients, it will be affected. We observe this, for example, in the region from 10^{-3} to 10^{-5} bar,

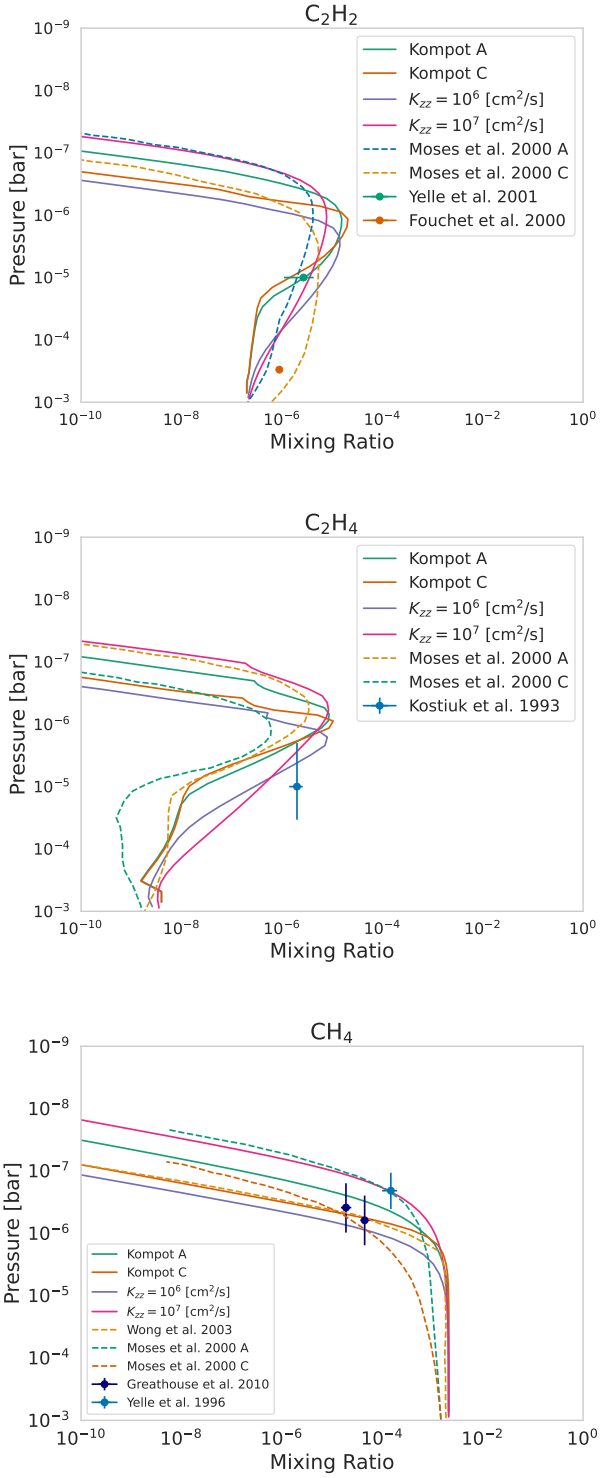

Fig. 5. Chemical profiles of C_2H_2, C_2H_4, and CH_4, together with measurements and the results from Moses et al. (2005). The solid lines represent the results from the Kompot Code, and the dashed lines show results from other models. The error bars are as follows, Yelle (2001) are measurements by the IRSHELL (Infrared Cryogenic Echelle Spectrograph), Fouchet et al. (2000) observed with ISO-SWS (Short Wave Spectrometer on the Infrared Space Observatory), Kostiuk et al. (1993) used IRHS (Infrared Heterodyne Spectrometer) at IRTF (NASA Infrared Telescope Facility), Greathouse et al. (2010) used the NH-UVS (New Horizons Alice UV Spectrometer), Seiff et al. (1996) used in situ measurement from Galileo. Please note that the plots do not include the ghost cells at the bottom boundary, which are kept constant during the simulation.

where the models differ most, leading to increased conduction in the two constant K_{zz} models. The initial jump in conduction heating can explain why both of the constant K_{zz} models are hotter in Fig. 2. This jump is a response to the lower boundary incoming heat flux, which accounts for around ~200 TW. In the same region, we also observe an increase in cooling from the constant K_{zz} models, particularly with $K_{zz} = 10^7$ cm/s. The increased cooling is mainly a result of radiative cooling from CH_4, which exhibits a jump due to its temperature and number density dependence.

3.2. Composition profiles

Figures 5 and 6 show the vertical mixing ratio profiles (without ghost cells) of the main hydrocarbons together with H and He, compared to the photochemical model of Moses et al. (2005) and available observations. There is good agreement with both other models and available observations, especially on crucial points such as the location of the homopause for CH_4 and the shapes of the profiles for minor hydrocarbons.

To explain the shapes of the main hydrocarbon profiles shown, we first need to establish the role of CH_4 as the parent molecule. The main pathways to the C_2-bearing molecules are recombination reactions containing the radical CH_3. An abundance of CH_3 is initiated right below the homopause, due to the fast photolysis of CH_4 by solar UV photons. It then disappears because turbulent mixing is not strong enough to carry it higher, and because reactions with other hydrocarbons form additional hydrocarbons. This localised high mixing ratio of CH_3 helps the formation of heavier hydrocarbons around the homopause, and we see clear peaks in all of the C_2 bearing species in Figs. 5 and 6.

The atomic hydrogen abundance experiences a sharp rise up until the μbar level, indicating the onset of ion-neutral chemistry, eventually leading to the formation of H_2^+ and H_3^+. This is the effect of a combination of CH_4 photolysis and H_2 dissociation, which causes temperatures to drop at low pressures via infrared emission. As the helium abundance behaves as expected with altitude, i.e. staying constant until the homopause is reached, it can be used as a useful reference for how species unaffected by interactions with other species and only subject to diffusion behave.

3.3. Influence of Io

The main drivers of Jupiter's dynamics include planetary rotation, which is coupled with the magnetosphere via the conducting ionospheric layer in the upper atmosphere, the solar wind, and its moons, mainly Io (Al Saati et al. 2022).

Together with the magnetic field lines from Jupiter and the plasma release from Io's volcanic activity, a plasma torus forms around Jupiter, which can be observed via multiple ionic emission lines in the extreme ultraviolet (Bagenal et al. 2004). Moving on its orbit around Jupiter, Io also serves as a unipolar inductor (Goldreich & Lynden-Bell 1969), which accelerates some of the plasma from the torus towards the polar regions of Jupiter's ionosphere. These charged particles are accelerated to high energies and create footprints in the polar areas of Jupiter's ionosphere visible in X-rays and UV where they impact the planet (e.g. Bhardwaj & Gladstone 2000). This particle precipitation changes the local conditions in the ionosphere due to energy deposition and additional ionisation, which has an effect on local electrical conductivity and Joule heating (e.g. Bagenal & Dols 2020).

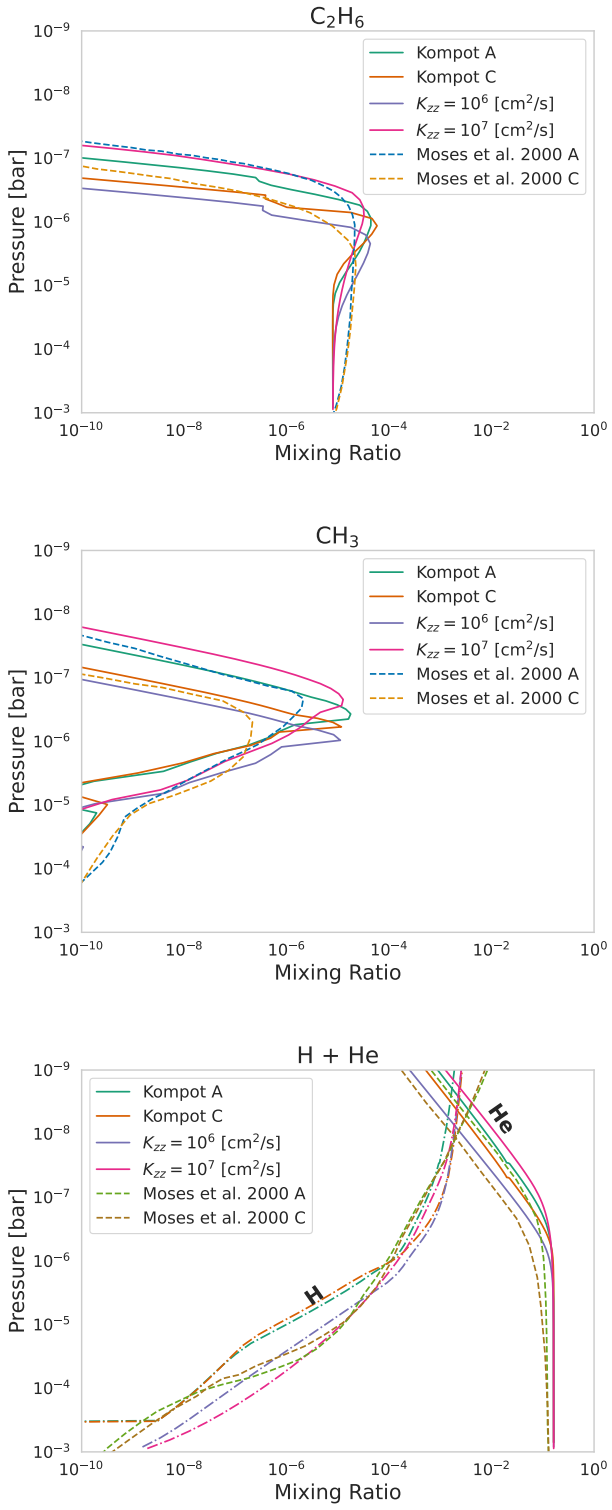

Fig. 6. Chemical profiles of hydrocarbons as well as H and He together with the model results from Moses et al. (2005). Please note that the plots do not include the ghost cells at the bottom boundary, which are kept constant during the simulation.

Since the Kompot code is a 1D model, the extent of magnetospheric effects it accounts for is limited to the total Joule heating deposited in the atmosphere, which is parametrised. The code does self-consistently calculate the Pedersen conductivity, but does not include the external influences, such as precipitating

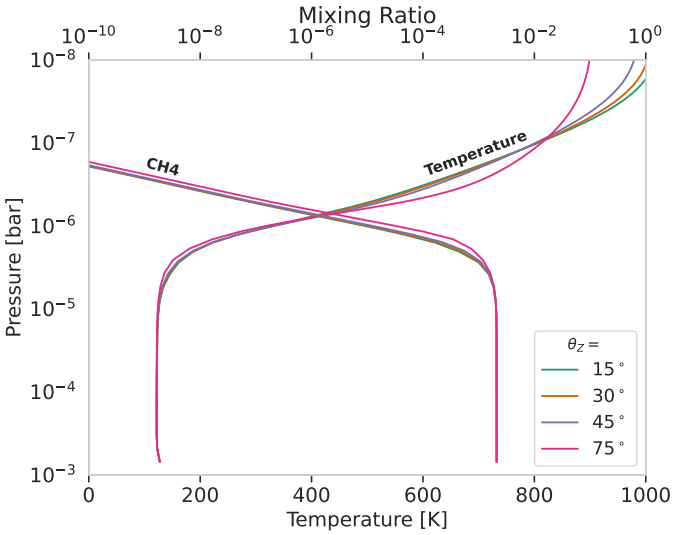

Fig. 7. Comparison of the model sensitivity to different zenith angles. Impact on both mixing ratio profile of CH_4 and the thermal profile is shown for four different values of the zenith angle (coloured lines).

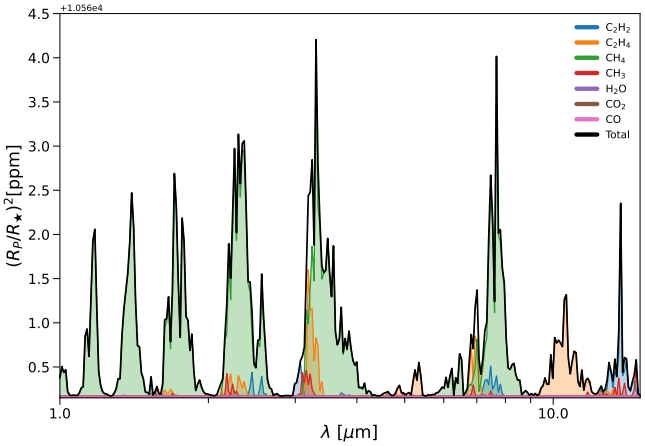

Fig. 8. The transmission spectrum of Jupiter as seen between 1 and 15 μm calculated from Model A. Most of the contributions come from 0.1 to 1 mbar. The shaded regions describe absorption contributions from different species to the black line, which shows the total spectrum. Individual contributions from the CIA for H_2–H_2 and H_2–He, and from Rayleigh scattering, are intentionally omitted but still included in the total contributions. Please note that the y-axis values are shown relative to an offset of $+1.056 \times 10^4$.

particles. For this reason, additional analysis from magnetospheric models and observations would be required to better study Io's impact using our models.

3.4. Sensitivity to free parameters

Since lower boundary input molecular mixing ratios are the same in all models, constrained by several models and measurements (Moses et al. 2005, and references therein), we consider the free input parameters to be the eddy diffusion profile, total atmospheric Joule heating, and zenith angle. In Fig. 7, the results for different zenith angles with the other parameters fixed are shown. The only large-scale changes are in the top-most part of the atmosphere between 10^{-7} and 10^{-9} bars, where heating from XUV radiation dominates the energy balance. Globally, heating from XUV radiation is very minor compared to Joule heating, so the dominance of XUV heating comes from the absence of other effects. These differences are of the order of 100 K, still well within the limits of even the longitudinal deviations of Jupiter's temperature (Roberts et al. 2025). If we increase the total Joule heating by a factor of 2 beyond the values given in Table 1, we observe an increase of approximately 100 K. We deem this acceptable given the spatial irregularity and uncertainty in the magnitude of the Joule heating present (Nishida & Watanabe 1981; Bougher et al. 2005; Müller-Wodarg et al. 2025).

3.5. The role of eddy diffusion and the homopause

The homopause plays a significant role in shaping chemical profiles. Where the gas is well mixed, mixing ratios of most of the initially available chemical species stay relatively uniform until the homopause is reached. Above the homopause, the species densities fall off according to their scale height, which means that the number density of heavier species decays faster. This is especially true for CH_4, for which photolysis reactions start just below its homopause. The combination of photolysis and the smaller scale height leads to the steep gradient we see in Fig. 6.

A significant problem with eddy diffusion is that the coefficients vary substantially across objects and are notoriously difficult to constrain. In addition, they cannot be calculated analytically (Lindzen 1981; Strobel et al. 1985). Both profiles used in this work are relatively similar in the lower pressure range considered up to about 10^{-5} bar, where they diverge and differ by at most an order of magnitude.

Using constant eddy coefficients of 10^6 and 10^7 cm^2/s, we can illustrate the differences between a variable profile and a constant one and highlight the impact of an order-of-magnitude difference. The main divergence between the complex and constant K_{zz} models visible in Fig. 1, is the consistent under- versus overestimation of the chemical abundances and temperature, compared to those of the more complex eddy coefficient profiles.

3.6. Spectral features

Figure 8 shows a synthetic transmission spectrum of Jupiter as an exoplanet, assuming it orbits a solar-analogue star, calculated from Model A. The spectrum spans wavelengths from 1 to 15 μm and is binned onto a logarithmically spaced wavelength grid with 300 points. The contribution to the spectrum comes predominantly from altitudes around 10^{-3} bar and up, as this is the lower boundary of our simulation, and we assume clouds are present below this level. Consequently, species primarily residing in the troposphere, specifically NH_3 and H_2O, are absent from this synthetic transmission spectrum.

In the wavelength range between 1 and 10 μm, CH_4 produces the most prominent spectral features (Wildt 1937), while C_2H_2 dominates at wavelengths longer than 10 μm. Beyond the dominant absorbers, the spectrum also contains several weaker features that observers could resolve in exoplanet observations of Jupiter, depending on the noise level and spectral resolution.

A minor C_2H_4 feature appears at 5.3 μm, but this feature would likely lie below the noise level. The C_2H_4 feature at 6.9 μm would be challenging to detect independently due to its proximity to a weaker CH_4 feature at a similar wavelength. However, a sufficiently high spectral resolution could resolve both features, in which case a pronounced peak would indicate the presence of both species. Another resolution-dependent feature appears at 3.2 μm, left of the strong CH_4 absorption at

3.7 μm, where sufficient spectral resolution could separate C_2H_4 from CH_4. While C_2H_2 may be difficult to detect between 1 and 10 μm, its strong feature at 13.7 μm could be detectable under favourable noise conditions.

To place these results in context, we compare our synthetic spectrum to available observations of Jupiter's atmosphere. Near-infrared measurements obtained with XSHOOTER (Montañés-Rodríguez et al. 2015) show strong CH_4 absorption between 1 and 2.5 μm, in good agreement with the dominant methane features in our model. More specifically, we replicate the relative strength of the absorption bands, with the 2.3 μm feature being the deepest and the subsequent 1.7 μm, 1.4 μm, and 1.2 μm showing diminishing depth. Similarly, Kedziora-Chudczer & Bailey (2011) reports prominent CH_4 absorption bands between 1.6 and 1.9 μm, further supporting the robustness of methane as the primary absorber in this wavelength range. Montañés-Rodríguez et al. (2015) additionally report two absorption features at 1.5 and 2.0 μm, which they attribute to a layer of crystalline H_2O ice near the 0.5 mbar level. This pressure lies within our simulated domain, so its absence in our spectrum is not due to our lower boundary, as it is for NH_3 and tropospheric H_2O vapour. Rather, it reflects that our transmission spectrum calculation includes only gas-phase molecular opacity and does not account for aerosol or ice-cloud scattering. This suggests that a full accounting of Jupiter's near-infrared transmission spectrum, and by extension that of a cool gas giant exoplanet, requires aerosol microphysics in addition to gas-phase photochemistry and heating/cooling. Similarly, Irwin et al. (2014) find that CH_4 dominates a synthetic Jupiter transmission spectrum over 0.4–15 μm, computed using radiative transfer modelling. Their spectrum also shows increasing depth with each band between 1 and 10 μm in addition to a clear C_2H_4 feature around 7 μm. However, it is worth noting that the C_2H_4 feature at ∼ 10 μm is missing in their absorption spectrum.

A direct comparison with JWST data is difficult since only emission spectra are currently available (Rodríguez-Ovalle et al. 2024; Melin et al. 2024; Harkett et al. 2024). We can, however, test our photochemistry directly by comparing the modelled abundances of C_2H_2 and C_2H_6 against retrievals spanning a range of latitudes and techniques: JWST/MIRI observations of the southern auroral region (Rodríguez-Ovalle et al. 2024), disk-averaged Voyager/Cassini-CIRS retrievals (Nixon et al. 2007), ground-based IRTF/TEXES global maps (Fletcher et al. 2016), and Gemini-N/TEXES polar profiles. Our modelled C_2H_2 profile mixing ratio peaks at 2×10^{-5} near 10^{-6} bar, which is a few times higher than in Sinclair et al. (2023), about twice as much as the normal retrieval from Nixon et al. (2007), but matching their fixed troposphere retrieval well. C_2H_6 shows best agreement with the normal retrieval from Nixon et al. (2007), and less peak agreement with their more turbulent fixed troposphere profile. The retrieved values of C_2H_6 from Sinclair et al. (2023) also agree well in both shape and value with our model. This is consistent with the two species' differing photochemical lifetimes. C_2H_6 is comparatively inert, with a longer photochemical lifetime (Moses et al. 2005), making it well-mixed and largely insensitive to the local photochemical state. That our 1D model reproduces both species well across this spread of observations suggests that it is robust outside of regions with strong localised forcing.

4. Summary and conclusions

This work presents the first application of the Kompot model to Jupiter's upper atmosphere, extending a 1D first-principles framework to self-consistently simulate the average thermal and chemical structure between 10^{-3} and 10^{-10} bar. Treating Jupiter as an exoplanet orbiting a Sun-like star, we produce a globally averaged radial profile benchmarked against Galileo in situ measurements, JUNO/JIRAM retrievals, ground-based observations, and several models. We also present a synthetic transmission spectrum calculated between 1 and 15 μm using the TauREx radiative transfer code. With minor adjustments to the chemical network to fit the higher temperatures of extrasolar gas giants (planned for future work), the model can be extended to simulate the upper atmospheres of hot and warm Jupiters. The key takeaways are summarised below:

- Kompot performs well in reproducing average chemical and thermal profiles similar to measurements as well as photochemical models in the literature. Our model also reproduces the observed vertical distributions of the main hydrocarbons in the upper atmosphere and the location of the homopause across the models;
- Eddy diffusion coefficients influence the overall profile of Jupiter's chemistry and thermal structure. The large differences highlight the importance of handling diffusion with care;
- According to our average model, the primary heating mechanism throughout most of the upper atmosphere of Jupiter is Joule heating. Close to the exosphere, at around 10^{-8} bar, it is overtaken by XUV driven heating. The main source of cooling below the homopause is radiative cooling by CH_4, which switches to H_3^+ line cooling in the heterosphere;
- Assuming a thick cloud deck at 1 mbar, many of the spectral features observable in the IR and mid-IR other than CH_4 would be difficult to detect in transmission spectroscopy as CH_4 dominates the spectrum in this wavelength range. Some features of minor hydrocarbons would be detectable depending on resolution and noise levels.

Acknowledgements. This work was carried out as part of the APPLE-Kompot ASAP project, supported by the Austrian Forschungsförderungsgesellschaft (FFG) funded through BMIMI.

References

Abel, M., Frommhold, L., Li, X., & Hunt, K. L. C. 2011, J. Phys. Chem. A, 115, 6805
Abel, M., Frommhold, L., Li, X., & Hunt, K. L. C. 2012, J. Chem. Phys., 136, 044319
Adam, A. Y., Yachmenev, A., Yurchenko, S. N., & Jensen, P. 2019, J. Phys. Chem. A, 123, 4755
Al-Refaie, A. F., Changeat, Q., Waldmann, I. P., & Tinetti, G. 2021, ApJ, 917, 37
Al-Refaie, A. F., Changeat, Q., Venot, O., Waldmann, I. P., & Tinetti, G. 2022, ApJ, 932, 123
Al Saati, S., Clément, N., Louis, C., et al. 2022, JGR (Space Phys.), 127, e2022JA030586
Amundsen, D. S., Baraffe, I., Tremblin, P., et al. 2014, A&A, 564, A59
Bagenal, F., & Dols, V. 2020, JGR (Space Phys.), 125, e27485
Bagenal, F., Downling, T. E., & McKinnonm, W. B. 2004, Jupiter: The Planet, Satellites and Magnetosphere (Cambridge, UK: Cambridge University Press)
Banks, P. M., & Kockarts, G. 1974, Science, 186, 1200
Baudino, J.-L., Bézard, B., Boccaletti, A., et al. 2015, A&A, 582, A83
Bell, T. J., Welbanks, L., Schlawin, E., et al. 2023, Nature, 623, 709
Bhardwaj, A., & Gladstone, G. R. 2000, Rev. Geophys., 38, 295
Bougher, S. W., Waite, J. H., Majeed, T., & Gladstone, G. R. 2005, JGR (Planets), 110, 2003JE002230
Chapman, S., & Cowling, T. G. 1960, Mathematical theory of non-uniform gases an account of the kinetic theory of viscosity, thermal conduction and diffusion in gases
Chubb, K. L., Tennyson, J., & Yurchenko, S. N. 2020, MNRAS, 493, 1531
Chubb, K. L., Rocchetto, M., Yurchenko, S. N., et al. 2021, A&A, 646, A21
Claire, M. W., Sheets, J., Cohen, M., et al. 2012, ApJ, 757, 95

Connerney, J. E. P., Kotsiaros, S., Oliversen, R. J., et al. 2018, Geophys. Res. Lett., 45, 2590
Cox, A. N. 2015, Allen's Astrophyiscal Quantities (Springer)
Dinelli, B. M., Adriani, A., Mura, A., et al. 2019, Phil. Trans. R. Soc. A, 377, 20180406
Fletcher, L. N., Greathouse, T. K., Orton, G. S., et al. 2016, Icarus, 278, 128
Fletcher, L. N., Gustafsson, M., & Orton, G. S. 2018, ApJS, 235, 24
Foster, J. C., St.-Maurice, J.-P., & Abreu, V. J. 1983, J. Geophys. Res., 88, 4885
Fouchet, T., Lellouch, E., Bézard, B., et al. 2000, A&A, 355, L13
Fox, J. L. 2015, Icarus, 252, 366
García Muñoz, A., Koskinen, T. T., & Lavvas, P. 2018, in Handbook of Exoplanets, eds. H. J. Deeg, & J. A. Belmonte (Springer International Publishing), 52
García-Melendo, E., Arregi, J., Rojas, J., et al. 2011, Icarus, 211, 1242
García Muñoz, A. 2007, PSS, 55, 1426
Gardner, J. P., Mather, J. C., Abbott, R., et al. 2023, PASP, 135, 068001
Gladstone, G., Allen, M., & Yung, Y. 1996, Icarus, 119, 1
Goldreich, P., & Lynden-Bell, D. 1969, ApJ, 156, 59
Gordon, I. E., Rothman, L. S., Hargreaves, R. J., et al. 2022, J. Quant. Spectrosc. Radiat. Transfer, 277, 107949
Grant, D., Lothringer, J. D., Wakeford, H. R., et al. 2023, ApJ, 949, L15
Greathouse, T. K., Gladstone, G., Moses, J., et al. 2010, Icarus, 208, 293
Grodent, D., Waite, J. H., & Gérard, J. 2001, JGR (Space Phys.), 106, 12933
Harkett, J., Fletcher, L. N., King, O. R. T., et al. 2024, JGR (Planets), 129, e2024JE008415
Herbst, E. 1985, ApJ, 291, 226
Horanyi, M., Cravens, T. E., & Waite, J. H. 1988, JGR (Space Phys.), 93, 7251
Huebner, W., & Mukherjee, J. 2015, PSS, 106, 11
Irwin, P. G. J., Barstow, J. K., Bowles, N. E., et al. 2014, Icarus, 242, 172
Johnstone, C. P. 2020, ApJ, 890, 79
Johnstone, C. P., Güdel, M., Lammer, H., & Kislyakova, K. G. 2018, A&A, 617, A107
Johnstone, C. P., Khodachenko, M. L., Lüftinger, T., et al. 2019, A&A, 624, L10
Johnstone, C. P., Lammer, H., Kislyakova, K. G., Scherf, M., & Güdel, M. 2021, EPSL, 576, 117197
JWST Transiting Exoplanet Community Early Release Science Team, Ahrer, E.-M., Alderson, L., et al. 2023, Nature, 614, 649
Kaspi, Y., Galanti, E., Hubbard, W. B., et al. 2018, Nature, 555, 223
Kasting, J. F., & Pollack, J. B. 1983, Icarus, 53, 479
Kedziora-Chudczer, L., & Bailey, J. 2011, MNRAS, 414, 1483
Kim, S. J., Sim, C. K., Geballe, T. R., et al. 2020, Icarus, 348, 113852
Knížek, A., Rimmer, P. B., & Ferus, M. 2026, Icarus, 444, 116806
Kostiuk, T., Romani, P., Espenak, F., Livengood, T. A., & Goldstein, J. J. 1993, JGR (Planets), 98, 18823
Kumer, J. B., & James, T. C. 1974, JGR, 79, 638
Li, G., Gordon, I. E., Rothman, L. S., et al. 2015, ApJS, 216, 15
Lindzen, R. S. 1981, JGR (Oceans), 86, 9707
Majeed, T., Waite, J. H., Bougher, S. W., & Gladstone, G. R. 2005, JGR (Planets), 110, 2004JE002351
Mant, B. P., Yachmenev, A., Tennyson, J., & Yurchenko, S. N. 2018, MNRAS, 478, 3220
Matcheva, K. I., & Strobel, D. F. 1999, Icarus, 140, 328
Melin, H., O'Donoghue, J., Moore, L., et al. 2024, Nat. Astron., 8, 1000
Miller, S., Achilleos, N., Ballester, G. E., et al. 1997, Icarus, 130, 57
Miller, S., Stallard, T., Tennyson, J., & Melin, H. 2013, J. Phys. Chem. A, 117, 9770
Montañés-Rodríguez, P., González-Merino, B., Pallé, E., López-Puertas, M., & García-Melendo, E. 2015, ApJ, 801, L8
Moses, J. I., Fouchet, T., Bézard, B., et al. 2005, JGR (Planets), 110, 2005JE002411
Murray-Clay, R. A., Chiang, E. I., & Murray, N. 2009, ApJ, 693, 23
Müller-Wodarg, I. C. F., Iñurrigarro, P., Moore, L., Koskinen, T. T., & Medvedev, A. S. 2025, ApJ, 990, L22
Nishida, A., & Watanabe, Y. 1981, JGR (Space Phys.), 86, 9945
Nixon, C. A., Achterberg, R. K., Conrath, B. J., et al. 2007, Icarus, 188, 47
Oberheide, J., Mlynczak, M. G., Mosso, C. N., et al. 2013, JGR (Space Phys.), 118, 7283
Perry, J. J., Kim, Y. H., Fox, J. L., & Porter, H. S. 1999, JGR (Planets), 104, 16541
Polyansky, O. L., Kyuberis, A. A., Zobov, N. F., et al. 2018, MNRAS, 480, 2597
Raynaud, E., Lellouch, E., Maillard, J.-P., et al. 2004, Icarus, 171, 133
Richards, P. G., & Voglozin, D. 2011, JGR (Space Phys.), 116
Roberts, K., Moore, L., O'Donoghue, J., et al. 2025, PSJ, 6, 92
Rodríguez-Ovalle, P., Fouchet, T., Guerlet, S., et al. 2024, JGR (Planets), 129, e2024JE008299
Romani, P. N., Jennings, D. E., Bjoraker, G. L., et al. 2008, Icarus, 198, 420
Rothman, L. S., Gordon, I. E., Barber, R. J., et al. 2010, J. Quant. Spectrosc. Radiat. Transfer, 111, 2139
Sandu, A., Verwer, J., Blom, J., et al. 1997, Atmos. Environ., 31, 3459
Schleich, S., Boro Saikia, S., Changeat, Q., et al. 2024, A&A, 690, A336
Schunk, R. W., & Nagy, A. F. 1978, Rev. Geophys., 16, 355
Schunk, R., & Nagy, A. 2009, Ionospheres: Physics, Plasma Physics, and Chemistry (Cambridge University Press), 72
Seiff, A., Kirk, D. B., Knight, T. C. D., et al. 1996, Science, 272, 844
Sinclair, J. A., Greathouse, T. K., Giles, R. S., et al. 2020, PSJ, 1, 85
Sinclair, J. A., Greathouse, T. K., Giles, R. S., et al. 2023, PSJ, 4, 76
Stallard, T. 2002, Icarus, 156, 498
Strobel, D. F. 1973, J. Atmos. Sci., 30, 489
Strobel, D. F., Apruzese, J. P., & Schoeberl, M. R. 1985, JGR (Atmos.), 90, 13067
Tennyson, J., Hulme, K., Naim, O. K., & Yurchenko, S. N. 2016, J. Phys. B, 49, 044002
Tennyson, J., Yurchenko, S. N., Al-Refaie, A. F., et al. 2020, J. Quant. Spectrosc. Radiat. Transfer, 255, 107228
Tennyson, J., Yurchenko, S. N., Zhang, J., et al. 2024, The 2024 release of the ExoMol database: molecular line lists for exoplanet and other hot atmospheres
Tremblin, P., Amundsen, D. S., Mourier, P., et al. 2015, ApJ, 804, L17
Tsai, S.-M., Lyons, J. R., Grosheintz, L., et al. 2017, ApJS, 228, 20
Tsai, S.-M., Lee, E. K. H., Powell, D., et al. 2023, Nature, 617, 483
Wakelam, V., Herbst, E., Loison, J.-C., et al. 2012, ApJS, 199, 21
Wildt, R. 1937, ApJ, 86, 321
Yelle, R. 2001, Icarus, 152, 331
Young, L. A., Yelle, R. V., Young, R., Seiff, A., & Kirk, D. B. 1997, Science, 276, 108
Yung, Y. L., Liang, M. C., Jiang, X., et al. 2009, JGR (Planets), 114, 2008JE003094
Yurchenko, S. N., Amundsen, D. S., Tennyson, J., & Waldmann, I. P. 2017, A&A, 605, A95
Yurchenko, S. N., Mellor, T. M., Freedman, R. S., & Tennyson, J. 2020, MNRAS, 496, 5282